Intermode-interaction-induced dynamics of continuous-variable quantum-key-distribution observables

Andrei Gaidash,[1,2,*] Alexei D. Kiselev,[2] George Miroshnichenko,[3,4] and Anton Kozubov[1,2]
[1]*Department of Mathematical Methods for Quantum Technologies, Steklov Mathematical Institute of Russian Academy of Sciences, 8 Gubkina Street, 119991 Moscow, Russia*
[2]*Laboratory of Quantum Processes and Measurements, ITMO University, 3b Kadetskaya Line, 199034 Saint Petersburg, Russia*
[3]*Waveguide Photonics Research Center, ITMO University, 49 Kronverksky Prospekt, 197101 Saint Petersburg, Russia*
[4]*Institute "High School of Engineering," ITMO University, 49 Kronverksky Prospekt, 197101 Saint Petersburg, Russia*

(Received 23 October 2023; accepted 10 June 2024; published 21 June 2024)

We theoretically study the dynamical regimes of the observables that govern the operating conditions of continuous-variable (CV) quantum-key-distribution (QKD) systems, depending on quantum-channel-induced intermode interactions. In contrast to the widely used approach in which losses and thermal broadening are introduced through a beam-splitter transformation, our analysis uses the exactly solvable quantum channel model describing the Lindblad dynamics of multimode bosonic systems interacting with a heat bath and additionally takes into account imperfections of the homodyne-detection scheme. The analytical results for the photon-count difference and the quadrature probability distributions are used to derive the expression for the mutual information between legitimate parties, which explicitly links the information properties of CV QKD and the parameters of the channel. For the important special case of a two-mode photonic system propagating in a fiber channel, the latter can be conveniently parameterized using the frequency and the relaxation-rate vectors that characterize the coherent (dynamical) intermode couplings and the incoherent (environment mediated) interaction between the bosonic modes, respectively. It turns out that these vectors determine four qualitatively different dynamical regimes of the mutual information and the phase difference between the signal and the local oscillator that may significantly affect the operation of CV QKD.

DOI: 10.1103/PhysRevA.109.062615

I. INTRODUCTION

Over the past decade, there has been a considerable surge of interest in the field of quantum information theory, especially quantum key distribution (QKD) [1–3]. Two distinct approaches for information encoding have emerged: discrete variables (DVs) that involve a discrete set of quantum states [4–11] and continuous variables (CVs) that exploit the continuous properties of quantum systems, such as the quadrature amplitudes of electromagnetic fields [12–22]. For both the DV and CV systems, the study of quantum state propagation in fiber channels faces notable challenges, predominantly stemming from decoherence and the intricacies of dynamical multimode interaction.

Decoherence arising from the interaction of quantum systems with the surrounding environment is known to be the principal source of disturbance (details can be found in foundational theoretical articles [23–25] and books [26,27] on the subject, along with papers dealing with fiber optics [28–32]). Quantum states propagating in fiber channels are influenced by a variety of effects. They include scattering, absorption, phase fluctuations, noise, and losses. In the context of multimode systems in which multiple modes are utilized to encode quantum information, phenomena like mode mixing and mode-dependent losses will additionally complicate the propagation dynamics. The intricate interplay between the quantum states and the environment can lead to mode-dependent decoherence (see, e.g., Ref. [33]), resulting in the degradation of the encoded information. Furthermore, decoherence phenomena impose limitations on the distance over which quantum states can be reliably transmitted through fiber channels.

In this paper, we focus our attention on the propagation of quantum states related to CV QKD observables through fiber channels [17,21,34–36]. In contrast to conventional approaches, in which losses and thermal broadening are introduced by a beam splitter, the model under consideration, a successor of our previous studies [31–33,37] on the dynamics of quantum states in the DV case, aims to investigate dynamical regimes of CV QKD observables governed by coherent (dynamical) intermode couplings and incoherent (environment mediated) interactions between the bosonic modes. To this end, we employ the general approach to the evolution of the Glauber-Sudarshan quasiprobability distribution (P function) [38,39] adapted to the fiber-channel framework.

In order to accurately characterize the interaction between the open quantum system and its surrounding environment, we employ the two-mode Liouville equation in the generalized Gorini-Kossakowski-Sudarshan-Lindblad form [40,41]. This equation enables us to model the dynamics and evolution of quantum states as they propagate through the fiber channel,

*Contact author: andrei_gaidash@itmo.ru

accounting for diverse environmental influences. Through this methodology, our objective is to attain a comprehensive understanding of the complex interaction between the quantum system and its environment. This endeavor will facilitate the enhancement of our knowledge of CV quantum state propagation and the development of effective strategies to mitigate the adverse effects introduced by the fiber-channel environment.

The structure of this paper is as follows. Preliminaries are provided in Sec. II, where we discuss the homodyne kernel, Liouville equation, and dynamics of the characteristic function. The main result is presented in Sec. III, which provides theoretical descriptions of the superpropagator, optical scheme of the CV QKD system, and the resulting dynamical model. The estimation of mutual information and analysis of dynamical regimes are described in Sec. IV. Section V concludes the paper.

II. PRELIMINARIES

In this section, we introduce essential concepts and definitions. This part of the paper provides building blocks for understanding subsequent theoretical considerations.

A. Homodyne kernel

In order to examine quadrature distribution, it is convenient to use the Glauber-Sudarshan P representation:

$$\hat{\rho} = \int P(\eta)|\eta\rangle\langle\eta| d^2\eta, \tag{1}$$

where $\hat{\rho}$ is the density matrix, $P(\eta)$ is the Glauber-Sudarshan quasiprobability distribution (P function), $|\eta\rangle$ is the coherent state with the complex-valued amplitude $\eta \in \mathbb{C}$, and the integral is performed over the complex plane, $d^2\eta = d\mathrm{Re}(\eta) d\mathrm{Im}(\eta)$. The quadrature distribution is closely related to the probability distribution of the photon-count difference $W_{n_{21}}$, which is measured using a homodyne-detection scheme and is given by [42]

$$W_{n_{21}} = \int K_{n_{21}}(\alpha, \beta) P_S(\alpha) P_{\mathrm{LO}}(\beta) d^2\alpha\, d^2\beta, \tag{2}$$

where $K_{n_{21}}(\alpha, \beta)$ is the kernel of homodyne detection and P_S and P_{LO} are P functions of the signal and the local oscillator, respectively. We can now use standard derivation technique to transform the kernel $K_{n_{21}}$ into the Gaussian form:

$$\begin{aligned} &K_{n_{21}}(\alpha, \beta) \\ &\quad = \sum_{n_1=0}^{\infty} |\langle n_1|(c\beta - s\alpha)k\rangle|^2 |\langle n_{21} + n_1|(s\beta + c\alpha)r\rangle|^2 \\ &\quad = \sum_{n_1=0}^{\infty} e^{-\mu} \frac{\mu^{n_1}}{n_1!} e^{-\lambda} \frac{\lambda^{n_{21}+n_1}}{(n_{21}+n_1)!} \\ &\quad \to \int_{-\infty}^{\infty} \frac{1}{2\pi\sqrt{\mu\lambda}} e^{\frac{-(n_1-\mu)^2}{2\mu}} e^{\frac{-(n_{21}+n_1-\lambda)^2}{2\lambda}} dn_1 \\ &\quad = \frac{1}{\sqrt{2\pi(\mu+\lambda)}} e^{-\frac{[n_{21}+(\mu-\lambda)]^2}{2(\mu+\lambda)}}, \end{aligned} \tag{3}$$

where n_1 and $n_2 = n_{21} + n_1$ are the photon counts registered by the corresponding detectors; $c = \cos\theta$ and $s = \sin\theta$ are the coefficients of the beam splitter, where the angle $0 < \theta < \frac{\pi}{2}$ takes the value $\theta = \pi/4$ for the case of a symmetric beam splitter; the coefficients $k \leqslant 1$ and $r \leqslant 1$ are related to imperfect detection so that k^2 and r^2 are the quantum efficiencies of the detectors; and the amplitudes μ and λ are given by

$$\mu = |c\beta - s\alpha)k|^2, \quad \lambda = |(s\beta + c\alpha)r|^2. \tag{4}$$

In Eq. (3) we utilized the Gaussian approximation for the Poisson distribution, which is justified provided the amplitudes μ and λ are sufficiently large. The latter holds in the case of a strong local oscillator (LO). It should be emphasized that another standard technique, where Gaussian approximation is applied to modified Bessel functions of the first kind, fails when detection imperfections and the asymmetry of the beam splitter are taken into account. After algebraic simplifications, the final form of the kernel is as follows:

$$K_{n_{21}}(\alpha, \beta) = \frac{\exp\left(-\frac{[n_{21} - Y|\beta|^2 - Z|\beta|(\alpha e^{-i\phi} + \mathrm{c.c.})]^2}{2X|\beta|^2}\right)}{\sqrt{2\pi X|\beta|^2}}, \tag{5}$$

where

$$\begin{aligned} X &= (k\cos\theta)^2 + (r\sin\theta)^2, \\ Y &= (k\cos\theta)^2 - (r\sin\theta)^2, \\ Z &= \frac{\sin(2\theta)(k^2 + r^2)}{2}. \end{aligned} \tag{6}$$

B. Liouville equation

Our task now is to investigate the effects of physical channel parameters on the probability distribution of the photon-count difference $W_{n_{21}}$. We also intend to establish a relation linking the probability distribution of the photon-count difference $W_{n_{21}}$ and the quadrature probability distribution W_Q.

To this end, we consider the two-mode Liouville equation:

$$\begin{aligned} \frac{\partial\hat{\rho}}{\partial t} = \hat{L}\hat{\rho} = &-i\sum_{n,m} \Omega_{nm}[\hat{a}_n^\dagger \hat{a}_m, \hat{\rho}] \\ &- \sum_{n,m} \Gamma_{nm}[(n_T + 1)(\hat{a}_n^\dagger \hat{a}_m \hat{\rho} + \hat{\rho}\hat{a}_n^\dagger \hat{a}_m - 2\hat{a}_m \hat{\rho} \hat{a}_n^\dagger) \\ &+ n_T(\hat{a}_m \hat{a}_n^\dagger \hat{\rho} + \hat{\rho}\hat{a}_m \hat{a}_n^\dagger - 2\hat{a}_n^\dagger \hat{\rho} \hat{a}_m)], \end{aligned} \tag{7}$$

where the indexes $m, n \in \{1, 2\}$ label the modes and the dagger denotes Hermitian conjugation; $\hat{\rho}$ is the density matrix representing a quantum state; $\hat{a}_n^\dagger$ ($\hat{a}_n$) is the creation (annihilation) operator of the nth mode; $[\hat{A}, \hat{B}] = \hat{A}\hat{B} - \hat{B}\hat{A}$ stands for the commutator; Ω (Γ) is the frequency (relaxation) matrix; and n_T is the mean number of thermal photons, given by

$$n_T = \frac{1}{e^{\frac{\hbar\Omega_0}{k_B T}} - 1}, \tag{8}$$

where Ω_0 is the free-space (bare) frequency, $\hbar$ is the reduced Planck constant, k_B is the Boltzmann constant, and T is the temperature of the environment. Frequency and relaxation matrices are both Hermitian, $\Omega = \Omega^\dagger$ and $\Gamma = \Gamma^\dagger$, and describe the coherent (dynamical) intermode coupling and incoherent (environment mediated) interactions between the bosonic modes, respectively. In the two-mode (polarization)

case, they can be defined using the Pauli matrices as follows:

$$\Omega = \tfrac{1}{2}[\omega_0\sigma_0 + (\boldsymbol{\omega}, \boldsymbol{\sigma})], \quad \Gamma = \tfrac{1}{2}[\gamma_0\sigma_0 + (\boldsymbol{\gamma}, \boldsymbol{\sigma})], \tag{9}$$

where $(\cdot\,,\,\cdot)$ stands for the scalar product; σ_0 is the identity matrix; ω_0 and γ_0 are the mean bare optical frequency and the mean relaxation rate, respectively; $\boldsymbol{\sigma} = (\sigma_1, \sigma_2, \sigma_3)$, where σ_i is the Pauli matrix; and $\boldsymbol{\omega} = (\omega_1, \omega_2, \omega_3)$ [$\boldsymbol{\gamma} = (\gamma_1, \gamma_2, \gamma_3)$] is the frequency (relaxation) vector. The vectors $\boldsymbol{\omega}$ and $\boldsymbol{\gamma}$ encode channel anisotropy parameters: the eigenvectors and eigenvalues of the anisotropic part of the matrix Ω (Γ) determine the orientation of the principal axes and the principal values describing the birefringence (the dichroism or polarization-dependent losses). In addition, the relaxation matrix Γ giving the rates of thermalization should be positive definite, $\Gamma > 0$. It is not difficult to show that the latter can be equivalently formulated as the inequality for the relaxation rates: $\gamma_0 > |\boldsymbol{\gamma}|$. An important point is that the matrices Ω and Γ both depend on the basis in the two-dimensional space of the polarization vectors and at least one of them may be diagonalized by choosing an appropriate basis.

C. Dynamics of characteristic function

In this section, closely following Ref. [43] [see Eqs. (16) and (24)], we present analytical results describing the evolution of normally ordered characteristic functions. According to Ref. [43], for the characteristic function of the initial state $\hat{\rho}_0$,

$$\begin{aligned}\chi_0(\boldsymbol{\alpha}) &= \mathrm{Tr}(e^{(\boldsymbol{\alpha},\hat{\boldsymbol{a}}^\dagger)}e^{-(\boldsymbol{\alpha}^*,\hat{\boldsymbol{a}})}\hat{\rho}_0)\\ &= \int dg(\boldsymbol{\beta})e^{(\boldsymbol{\alpha}^*,\boldsymbol{\beta})-(\boldsymbol{\alpha},\boldsymbol{\beta}^*)}P(\boldsymbol{\beta}, 0),\end{aligned} \tag{10}$$

where

$$\boldsymbol{\alpha} = \{\alpha_1, \alpha_2, \dots\}, \quad f(\boldsymbol{\alpha}) = f(\alpha_1, \alpha_2, \dots, \alpha_1^*, \alpha_2^*, \dots), \tag{11}$$

$$(\boldsymbol{a}, \boldsymbol{b}) = \sum_i a_i b_i, \quad dg(\boldsymbol{\beta}) = \prod_i \frac{d^2\beta_i}{\pi}, \tag{12}$$

$$\hat{\rho}_0 = \int P(\boldsymbol{\beta}, 0)|\boldsymbol{\beta}\rangle\langle\boldsymbol{\beta}|dg(\boldsymbol{\beta}), \tag{13}$$

the temporal evolution of the characteristic function is governed by the following relation:

$$\begin{aligned}\chi(\boldsymbol{\alpha}, t) &= \mathrm{Tr}[e^{(\boldsymbol{\alpha},\hat{\boldsymbol{a}}^\dagger)}e^{-(\boldsymbol{\alpha}^*,\hat{\boldsymbol{a}})}\hat{\rho}(t)]\\ &= e^{-[\boldsymbol{\alpha}^*,\boldsymbol{B}(t)\boldsymbol{\alpha}]}\chi_0(\boldsymbol{A}(t)\boldsymbol{\alpha}),\end{aligned} \tag{14}$$

where

$$\boldsymbol{A}(t) = e^{(i\Omega-\Gamma)t}, \quad \boldsymbol{B}(t) = n_T[\boldsymbol{I} - \boldsymbol{A}(t)^\dagger\boldsymbol{A}(t)], \tag{15}$$

and $\boldsymbol{I}$ is the identity matrix of appropriate size. For the two-mode bosonic system, it is not difficult to obtain the explicit expression for the matrix $\boldsymbol{A}(t)$:

$$\boldsymbol{A}(t) = e^{-(i\omega_0+\gamma_0)t}\left(\cosh(qt)\sigma_0 - \frac{\sinh(qt)}{q}(\boldsymbol{\gamma} + i\boldsymbol{\omega}, \boldsymbol{\sigma})\right), \tag{16}$$

where

$$q = \sqrt{(\boldsymbol{\gamma} + i\boldsymbol{\omega}, \boldsymbol{\gamma} + i\boldsymbol{\omega})} = \sqrt{|\boldsymbol{\gamma}|^2 - |\boldsymbol{\omega}|^2 + 2i(\boldsymbol{\gamma}, \boldsymbol{\omega})}. \tag{17}$$

III. DYNAMICS OF PHOTON-COUNT DIFFERENCE AND QUADRATURE PROBABILITY DISTRIBUTION

In this section, we derive the general form of the superpropagator and describe a generic CV QKD system, using it as an illustrative example. Within the proposed framework, we make an original contribution by providing a comprehensive description of the impact of environment-mediated effects on the information properties of continuous-variable quantum states.

A. Green's function

Now we can use Eq. (14) to derive the phase-space representation for the kernel of the Green's function, also known as the superpropagator, which governs the temporal evolution of the Glauber-Sudarshan P function given by Eq. (13). The Green's function is defined through the relation

$$P(\boldsymbol{\alpha}, t) = \int G(\boldsymbol{\alpha}, \boldsymbol{\beta}, t)P(\boldsymbol{\beta}, 0)dg(\boldsymbol{\beta}), \tag{18}$$

where $G(\boldsymbol{\alpha}, \boldsymbol{\beta}, t)$ is the kernel of the superpropagator. The Glauber-Sudarshan quasiprobability distribution is known to be related to the normally ordered characteristic function χ by the Fourier transformation [the inverse relation is given by Eq. (10)]

$$P(\boldsymbol{\alpha}, t) = \int e^{(\boldsymbol{\eta},\boldsymbol{\alpha}^*)-(\boldsymbol{\eta}^*,\boldsymbol{\alpha})}\chi(\boldsymbol{\eta}, t)dg(\boldsymbol{\eta}). \tag{19}$$

We can now substitute Eq. (14) into Eq. (19) and use relation (10) to derive the Fourier transform of the kernel $\tilde{G}(\boldsymbol{\eta}, \boldsymbol{\beta}, t)$, given by

$$\tilde{G}(\boldsymbol{\eta}, \boldsymbol{\beta}, t) = e^{n_T[|\boldsymbol{A}(t)\boldsymbol{\eta}|^2-|\boldsymbol{\eta}|^2]+(\boldsymbol{A}^*(t)\boldsymbol{\eta}^*,\boldsymbol{\beta})-(\boldsymbol{A}(t)\boldsymbol{\eta},\boldsymbol{\beta}^*)}, \tag{20}$$

where $|\boldsymbol{\alpha}|^2 = (\boldsymbol{\alpha}^*, \boldsymbol{\alpha}) = \sum_i |\alpha_i|^2$. After performing the Gaussian integral

$$G(\boldsymbol{\alpha}, \boldsymbol{\beta}, t) = \int e^{(\boldsymbol{\eta},\boldsymbol{\alpha}^*)-(\boldsymbol{\eta}^*,\boldsymbol{\alpha})}\tilde{G}(\boldsymbol{\eta}, \boldsymbol{\beta}, t)dg(\boldsymbol{\eta}), \tag{21}$$

we arrive at the final result for the Green's function:

$$G(\boldsymbol{\alpha}, \boldsymbol{\beta}, t) = \det[\boldsymbol{B}(t)^{-1}]e^{-(\boldsymbol{A}(t)^T\boldsymbol{\beta}^*-\boldsymbol{\alpha}^*,\boldsymbol{B}(t)^{-1}(\boldsymbol{A}(t)^\dagger\boldsymbol{\beta}-\boldsymbol{\alpha}))}. \tag{22}$$

This expression can now be used to study how the parameters of the channel that determine the matrices $\boldsymbol{A}(t)$ and $\boldsymbol{B}(t)$ will influence the probability distribution of photon-count difference $W_{n_{21}}$ and the quadrature distribution W_Q of homodyne detection. As an example, we concentrate on the CV QKD setup in which homodyne detection is the cornerstone technological solution.

B. Continuous-variable quantum-key-distribution setup

We consider the generic CV QKD setup illustrated in Fig. 1 (see, for instance, Refs. [3,44,45]). A laser is a source producing light in the horizontally polarized coherent state that splits on an unbalanced beam splitter (UBS) into two paths: a short path, where modulation of the signal takes place, and a long path, where the LO changes its polarization to orthogonal after passing through a half-wave plate with the axis aligned at 45° [in Fig. 1, it is indicated as a wave plate (WP)]. A polarization beam splitter (PBS) combines the signal and the

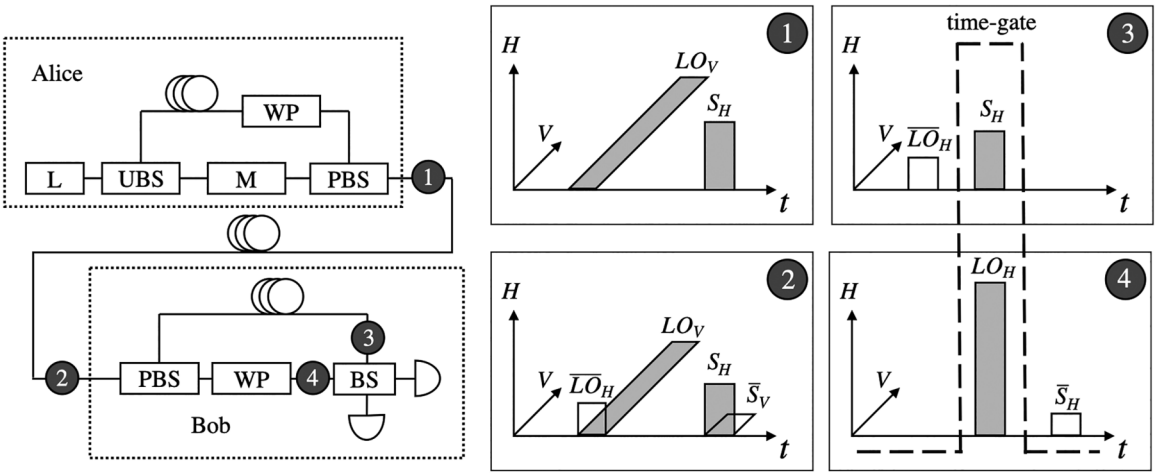

FIG. 1. Generic CV QKD scheme, where Alice (sender) and Bob (receiver) are outlined by the dotted lines, L is a laser, UBS is an unbalanced beam splitter, WP is a wave plate (specifically, it is a half-wave plate adjusted at 45°), M is a modulation device, PBS is a polarization beam splitter, and BS is a beam splitter. Also, polarization states of the signal and the LO (without scaling) are highlighted at several critical points of the scheme: Box 1 demonstrates the optical power of prepared states of the signal (denoted as S_H) and the LO (denoted as LO_V) at the entrance of a quantum channel. Box 2 demonstrates the signal and the LO at the entrance of the receiver; note that the polarization of the signal and the LO are perturbed during propagation, and we have designated additional parasitic fractions with an overline (i.e., $\overline{S}_V$ and $\overline{LO}_H$). Boxes 3 and 4 demonstrate optical signals for the long and short paths, respectively, at the entrance to the homodyne-detection scheme, where the detectors' time gate is shown by a thick dashed line. Only optical pulses within the time gate are detected and contribute to the interference.

LO, which is delayed in time. After the PBS, the beams travel to the entrance of a quantum channel. So the input states of the quantum channel are given by (see Fig. 1, box 1)

$$\begin{aligned}\hat{\rho}_S &= |\alpha_0\rangle_H\langle\alpha_0| \otimes |0\rangle_V\langle 0|,\\ \hat{\rho}_{\rm LO} &= |0\rangle_H\langle 0| \otimes |\beta_0\rangle_V\langle\beta_0|,\end{aligned} \tag{23}$$

where the limiting case of the strong LO with $|\beta_0| \gg |\alpha_0|$ is realized using a UBS with a sufficiently high transmission-to-reflection ratio.

In the quantum channel, both the signal and the LO are affected by fluctuations related to the anisotropy of the propagating medium (see Fig. 1, box 2). After the quantum channel, the signal and the LO arrive at the receiver, where a PBS separates them into the short and long paths as well. Now the LO travels along the short path, and its polarization is rotated back to its initial state by a WP, whereas the signal propagates through the long path. Finally, the signal and the LO are combined on a beam splitter so that they can be detected by the homodyne-detection scheme (electrical signals registered by two detectors are subtracted).

It should be noted that the detectors apply a time gate to cut off noninterfering parts of the signal and the LO, as shown in boxes 3 and 4 in Fig. 1. In other words, only the H component of the signal and only the V component of the LO that arrive at the receiver (Fig. 1, box 2) should be taken into account in order to reduce the noise. Mathematically, this means that contributions of other polarization components to the density matrix should be traced out.

In what follows, we will concern ourselves with the case where $|\beta_0| \gg |\alpha_0|$ and $|\beta_0| \gg \sqrt{n_T}$. So the propagation of the LO can be approximated using the zero-temperature limit $n_T \to 0$, whereas the evolution of the weak signal is affected by thermalization.

The initial states of the signal and the LO are pure coherent states (23). According to Eq. (18), in this case, the P function is equal to the Green's function. After tracing out the contribution of vertically (horizontally) polarized components to the P function of the signal (the LO) P_S ($P_{\rm LO}$), we have

$$\begin{aligned}P_S(\alpha,t) &= G(\alpha,\alpha_0,t)\\ &= \int G(\boldsymbol{\alpha},\boldsymbol{\alpha}_0,t)d^2\alpha_V,\\ P_{\rm LO}(\beta,t) &= G(\beta,\beta_0,t)\\ &= \int G(\boldsymbol{\beta},\boldsymbol{\beta}_0,t)d^2\beta_H|_{n_T\to 0}\\ &= \delta[\boldsymbol{A}_{22}^{\dagger}(t)\beta_0-\beta],\end{aligned} \tag{24}$$

where $\boldsymbol{\alpha}=(\alpha_H,\alpha_V)\equiv(\alpha,\alpha_V)$, $\boldsymbol{\alpha}_0=(\alpha_0,0)$, $\boldsymbol{\beta}=(\beta_H,\beta_V)\equiv(\beta_H,\beta)$, and $\boldsymbol{\beta}_0=(0,\beta_0)$. Note that we have utilized the following partial trace identity:

$$\begin{aligned}{\rm Tr}_1(\hat{\rho}_{12}) &= {\rm Tr}_1\left(\int P(\eta_1,\eta_2)|\eta_1\rangle\langle\eta_1| \otimes |\eta_2\rangle\langle\eta_2|d^2\eta_1 d^2\eta_2\right)\\ &= \int P'(\eta_2)|\eta_2\rangle\langle\eta_2|d^2\eta_2,\end{aligned} \tag{25}$$

$$P'(\eta_2) = \int P(\eta_1,\eta_2)d^2\eta_1. \tag{26}$$

Note that the above-discussed scheme primarily serves as an example illustrating the potential of the proposed approach. An important point is that our approach is applicable to alternative configurations that may involve modifications, for example, to the local LO and different mutual polarization of the signal and the LO. So other optical schemes may be regarded as derivatives of the configuration under consideration. For instance, in the case of the local LO, the P function of the

local oscillator given by Eq. (24) should be replaced with its time-independent version: $P_{\mathrm{LO}}(\beta,t)\equiv\delta(\beta_0-\beta)$. Similarly, generalization to different mutual polarizations of the signal and the LO requires using the modified P function of the LO: $P_{\mathrm{LO}}(\beta,t)\equiv\delta[(U\boldsymbol{A}^{\dagger}(t)U^{\dagger})_{22}\beta_0-\beta]$, with a suitably chosen unitary U.

We conclude this section with remarks concerning the time and polarization multiplexing employed in the scheme. Specifically, time multiplexing is used to separate out parasitic polarization components of the signal and the LO, which are marked by an overline in boxes 3 and 4 in Fig. 1. In the worst-case scenario, the modes may interact due to polarization deviations in such a way that the powers of the signal and the LO become comparable. In this case, the strong LO approximation breaks down, and analysis of the problem may require more sophisticated analytical and numerical tools. Nevertheless, certain results of the paper, such as the expression for the kernel of the superpropagator and the general approach for the evaluation, could still be useful beyond the scope of the strong-LO limiting case. As far as polarization multiplexing is concerned, it represents the most straightforward and efficient method for separating the signal and the LO. The raw key-generation rate without polarization multiplexing is either constrained by the operational rate of an optical switch or will suffer an additional 3-dB loss introduced by the beam splitter.

C. Resulting model

We can now insert the expressions for the homodyne kernel (5) and the P functions (24) into Eq. (2) to evaluate the temporal dependence of the probability distribution of the photon-count difference The result is given by

$$W_{n_{21}}(t)=\frac{1}{\sqrt{2\pi\sigma^2}}\exp\left(\frac{-(n_{21}-\Delta-\mu)^2}{2\sigma^2}\right), \tag{27}$$

where

$$\begin{aligned}\mu&=Z|\tilde{\beta}|(\tilde{\alpha}e^{-i\phi}+\text{c.c.}),\quad \Delta=Y|\tilde{\beta}|^2,\\ \sigma&=\sqrt{a}|\tilde{\beta}|,\quad a=X+2Z^2\boldsymbol{B}_{11}(t),\\ \tilde{\alpha}&=\boldsymbol{A}_{11}^{\dagger}(t)\alpha_0,\quad \tilde{\beta}=\boldsymbol{A}_{22}^{\dagger}(t)\beta_0,\quad \phi=\arg[\boldsymbol{A}_{22}^{\dagger}(t)].\end{aligned} \tag{28}$$

The distribution (27) is the Gaussian function of n_{21}, with the mean and the variance equal to $\Delta+\mu$ and σ^2, respectively.

It is easy to verify that

$$\lim_{t\to 0}W_{n_{21}}(t)=K_{n_{21}}(\alpha_0,\beta_0), \tag{29}$$

as it should for the initial coherent states since

$$\lim_{t\to 0}\boldsymbol{A}_{ii}(t)=1, \tag{30}$$

$$\lim_{t\to 0}a=\lim_{t\to 0}[X+2Z^2\boldsymbol{B}_{11}(t)]=X. \tag{31}$$

Also, note that

$$\lim_{t\to\infty}a=X+2Z^2n_T. \tag{32}$$

As we mentioned before, the photon-count-difference probability distribution is closely related to the quadrature distribution. After performing renormalization as in Refs. [46,47], we derive the distribution in the following Gaussian form:

$$W_Q(t)=\frac{1}{\sqrt{2\pi(\sigma')^2}}\exp\left[\frac{-1}{2}\left(\frac{Q-\Delta'-\mu'}{\sigma'}\right)^2\right], \tag{33}$$

where

$$\begin{aligned}Q&=\frac{n_{21}}{Z|\boldsymbol{A}_{11}^{\dagger}(t)\tilde{\beta}|},\quad \Delta'=\frac{\Delta}{Z|\boldsymbol{A}_{11}^{\dagger}(t)\tilde{\beta}|},\\ \mu'&=\alpha_0e^{i[\arg(\boldsymbol{A}_{11}^{\dagger}(t)\boldsymbol{A}_{22}(t)]}+\text{c.c.},\\ (\sigma')^2&=\frac{2\boldsymbol{B}_{11}(t)}{|\boldsymbol{A}_{11}^{\dagger}(t)|^2}+\frac{X}{Z^2|\boldsymbol{A}_{11}^{\dagger}(t)|^2}.\end{aligned} \tag{34}$$

IV. INFLUENCE OF ANISOTROPY ON MUTUAL INFORMATION

In this section, we apply our theoretical results to assess the impact of the environment on the mutual information between the sender and the receiver. We also investigate the dynamical regimes of the relaxation rate and the phase difference between the signal and the LO.

A. Mutual information

For the protocol behind the CV QKD scheme, we assume that instead of a single initial coherent state $|\alpha_0\rangle$, Alice prepares an ensemble of coherent states that has the Gaussian distribution with variance V_α. Averaging W_Q over the Gaussian random variable α_0 results in the Gaussian distribution with the variance V given by the sum of variances:

$$V=V_\alpha+(\sigma')^2, \tag{35}$$

where the term $(\sigma')^2$ is associated with the excess noise. It should be emphasized that, owing to the additive property of Gaussian variances, the noise may contain additional contributions that, for instance, could be related to electronics. However, in order to highlight the impact, we consider only the noise induced by the fiber. According to the Shannon-Hartley formula (for instance, see [48]), mutual information is given by

$$I_{AB}=\log_2(1+R_{\mathrm{SN}})=\log_2\left(1+\frac{V_\alpha}{(\sigma')^2}\right), \tag{36}$$

where R_{SN} is the signal-to-noise ratio. Given the value of V_α, we can insert the variance given by Eq. (34) into formula (36) to deduce the expression for the mutual information:

$$I_{AB}=\log_2\left(1+\frac{|\boldsymbol{A}_{11}^{\dagger}(t)|^2V_\alpha}{1+2\boldsymbol{B}_{11}(t)+\left(\frac{X}{Z^2}-1\right)}\right), \tag{37}$$

$$\frac{X}{Z^2}=\frac{\left(\frac{k^2}{\sin^2\theta}+\frac{r^2}{\cos^2\theta}\right)}{(k^2+r^2)^2}, \tag{38}$$

where the denominator is written as the sum of three terms: the first term is the vacuum noise, the second term describes thermal broadening [recall $\lim_{t\to\infty}\boldsymbol{B}(t)_{11}=n_T$], and the last term arises from imperfections in the detection scheme. Formula (37) agrees very well with the well-known phenomenological model, giving mutual information in the

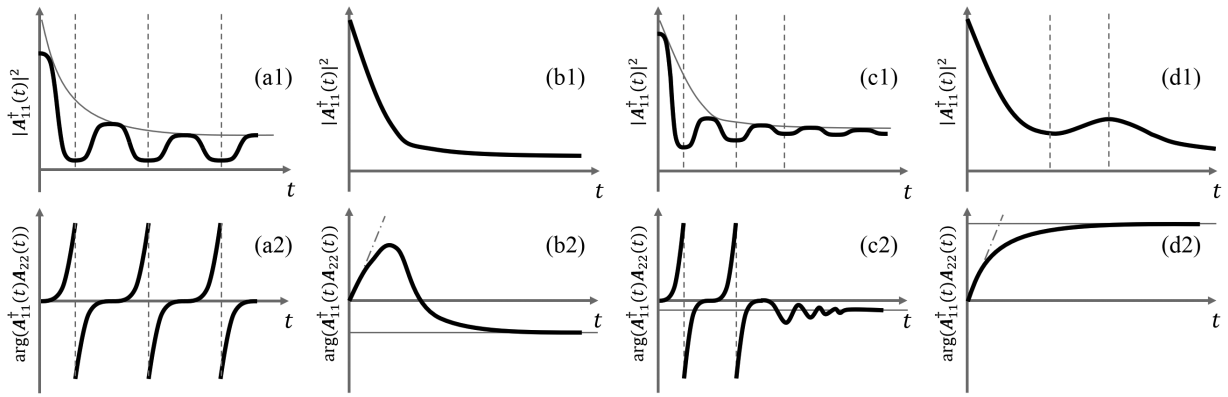

FIG. 2. Typical dependences of the relaxation rate $|A_{11}^{\dagger}(t)|^2$, defined by Eq. (40), and the phase difference between the signal and the LO $\arg[A_{11}^{\dagger}(t)A_{22}(t)]$, defined by Eq. (41), drawn as a sketch (without scaling) in order to highlight the principal differences between dynamical regimes. (a1) Relaxation rate when $|\boldsymbol{\omega}| \gg |\boldsymbol{\gamma}|$: exponential decay (shown as a solid gray line) modulated by harmonic oscillations (minimum coincidence with rapid phase-difference growth at the positions of the dashed gray lines). (a2) Nonlinear phase-difference growth (between $-\pi$ and π) when $|\boldsymbol{\omega}| \gg |\boldsymbol{\gamma}|$, equivalent to the phase of an ellipse. (b1) Relaxation rate when $|\boldsymbol{\omega}| \ll |\boldsymbol{\gamma}|$: multiexponential decay. (b2) The phase-difference growth when $|\boldsymbol{\omega}| \ll |\boldsymbol{\gamma}|$: almost linear dependence at the beginning (shown by the dash-dotted gray line), defined by Eq. (45), which then approaches the stationary value (shown by a solid gray line), defined by Eq. (46); it should be noted that the signs of the slope and stationary value may be coincident or not, as in this example. (c1) Relaxation rate when $|\boldsymbol{\omega}|$ is comparable to $|\boldsymbol{\gamma}|$, the intermediate case between the previous two with a smaller modulation depth. (c2) The phase difference when $|\boldsymbol{\omega}|$ is comparable to $|\boldsymbol{\gamma}|$: the same behavior as in the first case, approaching some stationary value after a time, defined by Eq. (48). (d1) Relaxation rate at the exceptional point when $|\boldsymbol{\gamma}| = |\boldsymbol{\omega}|$ and $\boldsymbol{\gamma} \perp \boldsymbol{\omega}$; nonexponential terms may result in nonmonotonic time dependence, leading to the presence of local extrema at $t = t_{\pm}$, denoted as dashed lines, according to Eq. (57). (d2) Almost linear growth of the phase difference at the beginning (shown by the dash-dotted gray line) with the rate $-2|\boldsymbol{\gamma}|t\sin(\varphi)$ and saturation values at $\pm\pi$ (here a positive value is shown by the solid gray line).

form

$$I_{AB} = \log_2\left(1 + \frac{e^{-\Gamma_0 t}V_\alpha}{1+2n_T}\right), \tag{39}$$

which represents the limiting case where effects of channel anisotropy and detection imperfections can be disregarded.

B. Dynamical regimes

According to Eq. (34), the dynamics of the quadrature distribution W_Q is determined by time-dependent parameters μ' and $(\sigma')^2$. The dynamics of these parameters is governed by the relaxation rate $|A_{11}^{\dagger}(t)|^2$ and the phase $\arg[A_{11}^{\dagger}(t)A_{22}(t)]$ that gives the phase difference between the signal and the LO. In this section, dynamical regimes of the relaxation rate and the phase will be our primary concern. It is generally expected that dynamics will reveal effects such as a deviation from exponential relaxation (a kind of modulation or multiexponential behavior) and nonlinear growth of the phase.

We begin with the explicit expressions for the rate and the phase, derived using Eq. (16). Let us take a closer look at these expressions:

$$|A_{11}^{\dagger}(t)|^2 = e^{-2\gamma_0 t}[c_1\cos(2bt) + c_2\cosh(2at) + c_3\sin(2bt) - c_4\sinh(2at)], \tag{40}$$

$$A_{11}^{\dagger}(t)A_{22}(t) = e^{-2\gamma_0 t}\{c_2\cos(2bt) + c_1\cosh(2at) + i[c_4\sin(2bt) + c_3\sinh(2at)]\}, \tag{41}$$

where

$$a = \mathrm{Re}(q), \quad b = \mathrm{Im}(q), \tag{42}$$

$$c_1 = \frac{1}{2}\left(1 - \frac{\omega_3^2+\gamma_3^2}{|q|^2}\right), \quad c_2 = \frac{1}{2}\left(1 + \frac{\omega_3^2+\gamma_3^2}{|q|^2}\right), \tag{43}$$

$$c_3 = \frac{a\omega_3 - b\gamma_3}{|q|^2}, \quad c_4 = \frac{b\omega_3 + a\gamma_3}{|q|^2}, \tag{44}$$

and q is given by Eq. (17). Clearly, the dynamical regime is governed by the following parameters: the relative lengths of the $\boldsymbol{\omega}$ and $\boldsymbol{\gamma}$ vectors, the angle between them, and the components ω_3 and γ_3. Investigation of the parametric dependence of $\mathrm{Re}[A_{11}^{\dagger}(t)A_{22}(t)]$ and $\mathrm{Im}[A_{11}^{\dagger}(t)A_{22}(t)]$ on time may provide useful insights into the $\arg\{\mathrm{Re}[A_{11}^{\dagger}(t)A_{22}(t)]\}$ behavior (the common factor $e^{-2\gamma_0 t}$ does not affect the phase and can be ignored).

Now we consider the following special dynamical regimes and related effects:

(1) The first case occurs when $b \gg a$ or, alternatively, $|\boldsymbol{\omega}| \gg |\boldsymbol{\gamma}|$ (at least by 1 order). The parametric dependence of $\mathrm{Re}[A_{11}^{\dagger}(t)A_{22}(t)]$ and $\mathrm{Im}[A_{11}^{\dagger}(t)A_{22}(t)]$ becomes an ellipse; then we expect to observe nonlinear growth of the phase, as shown in Fig. 2(a2). As eccentricity approaches unity, the relaxation oscillating "modulation" [shown in Fig. 2(a1)] becomes deeper. However, it may be observed only in the case of rather strong frequency anisotropy: $|\boldsymbol{\omega}| > \gamma_0$; otherwise, the effect is weak.

(2) The second case takes place when $a \gg b$ or, alternatively, $|\boldsymbol{\gamma}| \gg |\boldsymbol{\omega}|$ (at least by 1 order). Initially, the phase grows almost linearly [shown in Fig. 2(b2) as a dash-dotted gray line] as

$$2\left(\omega_3 - \frac{2b\gamma_3}{a}\right)t \tag{45}$$

and then becomes stationary with the approximate value [shown in Fig. 2(b2) as a solid gray line]

$$\arctan\left(\frac{2(a\omega_3 - b\gamma_3)}{a^2 - \gamma_3^2 - \omega_3^2}\right). \tag{46}$$

The relaxation rate can be approximately described by the following three terms:

$$|\boldsymbol{A}_{11}^{\dagger}(t)|^2 \approx \frac{1}{4|\boldsymbol{\gamma}|^2}\big[2\big(|\boldsymbol{\gamma}|^2 - \gamma_3^2\big)e^{-2\gamma_0 t} + (|\boldsymbol{\gamma}| - \gamma_3)^2 e^{-2(\gamma_0 - |\boldsymbol{\gamma}|)t} + (|\boldsymbol{\gamma}| + \gamma_3)^2 e^{-2(\gamma_0 + |\boldsymbol{\gamma}|)t}\big], \tag{47}$$

where multiexponential behavior is clearly seen [shown in Fig. 2(b1)]. Also, it should be noted that the contribution of γ_3 to the length of $\boldsymbol{\gamma}$ plays a crucial role; it governs the proportion of each relaxation rate. At the same time, the relation between γ_0 and $|\boldsymbol{\gamma}|$ determines the visibility of the multiexponential behavior.

(3) The third case, where $|\boldsymbol{\gamma}|$ is comparable to $|\boldsymbol{\omega}|$, is intermediate. Combination of the two motives of the previous cases regarding relaxation rate is quite obvious [shown in Fig. 2(c1)]. However, the same cannot be said regarding the phase difference behavior. The parametric dependence of $\mathrm{Re}[\boldsymbol{A}_{11}^{\dagger}(t)\boldsymbol{A}_{22}(t)]$ and $\mathrm{Im}[\boldsymbol{A}_{11}^{\dagger}(t)\boldsymbol{A}_{22}(t)]$ becomes a spiral, where harmonic terms define elliptic rotation and hyperbolic ones determine the position of the center of the ellipse. In other words, at small t we may observe nonlinear phase growth as in the first case because there are still windings around the coordinates center, and for a larger t it approaches some stationary value as in the second case, as shown in Fig. 2(c2). One may define the transition time between two regimes by solving the following equation:

$$[c_1 c_2 \cosh(2at) + c_1]^2 + [c_3 c_4 \sinh(2at)]^2 = 1. \tag{48}$$

(4) Finally, we consider the case where q vanishes, $q = 0$, which takes place when $|\boldsymbol{\gamma}| = |\boldsymbol{\omega}|$ and $\boldsymbol{\gamma} \perp \boldsymbol{\omega}$. This is the special regime known as the exceptional point [49]. In this limit, the matrix $\boldsymbol{A}$ takes the form

$$\boldsymbol{A}(t) = e^{-(i\omega_0 + \gamma_0)t}[\sigma_0 - (\boldsymbol{\gamma} + i\boldsymbol{\omega}, \boldsymbol{\sigma})t], \tag{49}$$

giving the relations

$$|\boldsymbol{A}_{11}(t)|^2 = e^{-2\gamma_0 t}\big[1 - 2\gamma_3 t + \big(\gamma_3^2 + \omega_3^2\big)t^2\big], \tag{50}$$

$$\boldsymbol{A}_{11}^{\dagger}(t)\boldsymbol{A}_{22}(t) = e^{-2\gamma_0 t}\big[1 + 2i\omega_3 t - \big(\gamma_3^2 + \omega_3^2\big)t^2\big], \tag{51}$$

which can be rewritten as follows:

$$|\boldsymbol{A}_{11}(t)|^2 = e^{-2\gamma_0 t}(1 - 2|\boldsymbol{\gamma}|t\cos\varphi + |\boldsymbol{\gamma}|^2 t^2), \tag{52}$$

$$\boldsymbol{A}_{11}^{\dagger}(t)\boldsymbol{A}_{22}(t) = e^{-2\gamma_0 t}(1 - 2i|\boldsymbol{\gamma}|t\sin\varphi - |\boldsymbol{\gamma}|^2 t^2), \tag{53}$$

where we have used the angular parametrization for the vectors $\boldsymbol{\gamma}$ and $\boldsymbol{\omega}$, given by

$$\boldsymbol{\gamma} = |\boldsymbol{\gamma}|(\sin\varphi\cos\xi, \sin\varphi\sin\xi, \cos\varphi), \tag{54}$$

$$\boldsymbol{\omega} = |\boldsymbol{\gamma}|(\cos\varphi\cos\xi, \cos\varphi\sin\xi, -\sin\varphi). \tag{55}$$

Nonexponential terms in Eq. (50) may result in nonmonotonic time dependence of $|\boldsymbol{A}_{11}(t)|^2$, leading to the presence of local extrema. The loci of the latter can be found by solving the stationary point equation

$$\frac{d}{dt}|\boldsymbol{A}_{11}(t)|^2 = 0, \tag{56}$$

with the roots, t_- and t_+, expressed as follows:

$$t_{\pm} = \frac{|\boldsymbol{\gamma}| + 2\gamma_0\cos\varphi \pm \sqrt{|\boldsymbol{\gamma}|^2 - 4\gamma_0^2\sin^2\varphi}}{2\gamma_0|\boldsymbol{\gamma}|}. \tag{57}$$

At $|\boldsymbol{\gamma}| > 2\gamma_0|\sin\varphi|$ and $\cos\varphi > 0$ ($\cos\varphi < 0$), we have two different real positive (negative) roots representing the local minimum and maximum located at $t = t_-$ and $t = t_+$, respectively. The roots coalesce into the point $\gamma_0 t_- = \gamma_0 t_+ = 1 + \sqrt{4\gamma_0^2/|\boldsymbol{\gamma}|^2 - 1}$ provided that $2\gamma_0|\sin\varphi| = |\boldsymbol{\gamma}|$. Also, the special solution is $t = t_+ = 0$ if $\varphi = \pm\pi$ and $|\boldsymbol{\gamma}| = \gamma_0$. In the case of two positive roots illustrated in Fig. 2(d1), the longest time interval with a positive time derivative of $|\boldsymbol{A}_{11}(t)|^2$ ranges from $t_- = |\boldsymbol{\gamma}|^{-1}$ to $t_+ = |\boldsymbol{\gamma}|^{-1} + \gamma_0^{-1}$ at $\varphi = 0$. Qualitatively, the phase behavior looks similar to that in the previous case: almost linear growth at the beginning, with the rate being approximately $-2|\boldsymbol{\gamma}|t\sin\varphi$ and the saturation value at $\pm\pi$ [see Fig. 2(d2)], except when $\sin\varphi = 0$ and the saturation value equals zero.

V. CONCLUSION AND DISCUSSION

In this paper, we have presented a derivation encompassing a comprehensive representation of the general form of the superpropagator $G(\boldsymbol{\alpha}, \boldsymbol{\beta}, t)$ given by Eq. (22). The superoperator profoundly governs the temporal evolution of the Glauber-Sudarshan P function in the context of intricate relaxation processes described by the Liouville equation (7). This result might be helpful in various fields of quantum optics.

We applied the superpropagator to P functions of the signal and the LO of the generic CV QKD scheme shown in Fig. 1 and deduced the expressions for the probability distribution of the photon-count difference $W_{n_{21}}$ [see Eq. (27)] and the corresponding quadrature probability distribution W_Q [see Eq. (33)]. These expressions incorporate effects induced by both the imperfections of a homodyne-detection scheme and the dynamics of a quantum channel. For instance, this model can predict changes in the mean $\mu + \Delta$ ($\mu' + \Delta'$) and the variance σ^2 [$(\sigma')^2$] of the probability distribution of the photon-count difference (the quadrature probability function) representing the cornerstone parameters of a CV QKD system as follows:

(1) The efficiencies k^2 and r^2 that enter the parameters X, Y, and Z given by Eqs. (6) take into account detection efficiency mismatch.

(2) The angle θ which enters X, Y, and Z describes the unbalanced beam splitter in the homodyne-detection scheme.

(3) The relaxation and polarization deviation of the signal amplitude ($|\alpha_0|$) and the LO ($|\beta_0|$) are characterized by $|\boldsymbol{A}_{11}^{\dagger}(t)|$ and $|\boldsymbol{A}_{22}^{\dagger}(t)|$ [the matrix $\boldsymbol{A}(t)$ is given by Eq. (15)], respectively, and their values are directly connected to characteristics of the channel given by Eqs. (9) and (16).

(4) The dynamics of the phase difference between the signal and the LO is governed by the angle $\arg[\boldsymbol{A}_{11}^{\dagger}(t)\boldsymbol{A}_{22}(t)]$.

(5) The mean of the distribution should be rearranged by Δ or Δ'.

(6) The term $2\boldsymbol{B}_{11}(t)$ describes thermal broadening of the variance.

Thus, according to the model, a joint impact of the imperfections of a homodyne-detection scheme and relaxation in the channel may be estimated.

Like in our previous papers [31–33,37], the investigation of how the information properties of the considered CV QKD system are connected to the physical parameters of the channel continued to be a subject of interest. Formula (37) gives the mutual information between the sender and the receiver as a function of $|\boldsymbol{A}_{11}^{\dagger}(t)|$ and $\boldsymbol{B}_{11}(t)$ and explicitly shows the above connection. This result agrees very well with conventional models and provides generalization to the cases in which various anisotropic effects are taken into consideration.

The stated above motivates our study of dynamical regimes. For this purpose, we chose the relaxation rate governed by $|\boldsymbol{A}_{11}^{\dagger}(t)|^2$ and the phase difference between the signal and the LO determined by the angle $\arg[\boldsymbol{A}_{11}^{\dagger}(t)\boldsymbol{A}_{22}(t)]$. These parameters play an important role in the estimation of the CV QKD performance. From Eq. (37) the relaxation rate describes the decay of the mutual information. As for the phase difference, it is preserved for an ensemble of initial states; i.e., any initial state obtains the same phase shift after a propagation. However, it may be crucial when discretization of the measurement outcomes takes place. Thus, predictions regarding the phase shift may be useful. We have found that there are four qualitatively different dynamical regimes: (1) the regime dominated by coherent interaction at $|\boldsymbol{\omega}| \gg |\boldsymbol{\gamma}|$ with prevailing oscillatory behavior [see Figs. 2(a1) and 2(a2)]; (2) the regime dominated by incoherent interaction at $|\boldsymbol{\omega}| \ll |\boldsymbol{\gamma}|$ with prevailing exponential-decay behavior [see Figs. 2(b1) and 2(b2)]; (3) the intermediate regime where $\boldsymbol{\omega}$ is comparable to $\boldsymbol{\gamma}$ and one may observe a dynamical transition between the above two cases [see Figs. 2(c1) and 2(c2)]; and (4) the regime at the exception point where $|\boldsymbol{\gamma}| = |\boldsymbol{\omega}|$, with $\boldsymbol{\gamma} \perp \boldsymbol{\omega}$, and the multiexponential function appears to be replaced by a combination of exponential and nonexponential functions [see Figs. 2(d1) and 2(d2)]. As a result, there is a variety of channel anisotropy configurations, leading to distinct dynamical regimes and nontrivial dependence of the CV QKD characteristics on the channel parameters. It should be mentioned that, for a more complicated CV QKD setup such as measurement-device-independent QKD (see, for instance, Refs. [3,50–55]), the influence of channel anisotropy might be even more crucial since signals that have evolved in time should interfere with each other.

We selected the CV QKD framework primarily for illustrative purposes in this study. This paper aims more towards fundamental aspects. This paper predominantly focused on the fundamental aspects within this framework. However, we believe that the proposed model has broader implications and potential applications beyond CV QKD, as the observables considered in our model may have relevance in various fields. For instance, the results could be beneficial for future metrological investigations of fiber-optic channels or quantum hacking attacks, particularly in light of the recent work in [56]. Regarding CV QKD, our previous study [33] investigated the dynamics of a covariance matrix, which is an essential element for estimating the secret key rate of CV QKD. Combining these results with the current research could lead to tighter bounds in the security analysis.

As shown above, the applicability of Lindblad-type models for studying quantum dynamics in the presence of correlations between the system and an environment suggests that they form a natural basis for a connection between the physical effects of an environment and the information properties of quantum states. In particular, the derived form of the superpropagator combined with a mathematical toolbox of bosonic channels can be extended well beyond the scope of a generic CV QKD protocol.

ACKNOWLEDGMENTS

This work of A.G. and A.K. (Sec. III) was funded by the Ministry of Science and Higher Education of the Russian Federation (Grant No. 075-15-2020-788). The work of A.G. and A.K. (Sec. IV) was supported by the Russian Science Foundation under Grant No. 20-71-10072 and performed at the Steklov Mathematical Institute of the Russian Academy of Sciences. This work of A. Kiselev was funded by the Ministry of Education and Science of the Russian Federation (Passport No. 2019-0903).

All authors contributed equally to the work.

[1] V. Scarani, H. Bechmann-Pasquinucci, N. J. Cerf, M. Dušek, N. Lütkenhaus, and M. Peev, The security of practical quantum key distribution, Rev. Mod. Phys. **81**, 1301 (2009).

[2] E. Diamanti, H.-K. Lo, B. Qi, and Z. Yuan, Practical challenges in quantum key distribution, npj Quantum Inf. **2**, 16025 (2016).

[3] S. Pirandola *et al.*, Advances in quantum cryptography, Adv. Opt. Photonics **12**, 1012 (2020).

[4] C. H. Bennett, Quantum cryptography, in *Proceedings of the IEEE International Conference on Computers, Systems, and Signal Processing* (IEEE, New York, 1984), pp. 175–179.

[5] C. H. Bennett, F. Bessette, G. Brassard, L. Salvail, and J. Smolin, Experimental quantum cryptography, J. Cryptol. **5**, 3 (1992).

[6] H.-K. Lo and J. Preskill, Security of quantum key distribution using weak coherent states with nonrandom phases, Quantum Inf. Comput. **8**, 431 (2007).

[7] C. Gobby, Z. Yuan, and A. Shields, Quantum key distribution over 122 km of standard telecom fiber, Appl. Phys. Lett. **84**, 3762 (2004).

[8] A. Gaidash, G. Miroshnichenko, and A. Kozubov, Subcarrier wave quantum key distribution with leaky and flawed devices, J. Opt. Soc. Am. B **39**, 577 (2022).

[9] J. Bogdanski, J. Ahrens, and M. Bourennane, Sagnac quantum key distribution and secret sharing, Proc. SPIE **7236**, 72360M (2009).

[10] X.-F. Mo, B. Zhu, Z.-F. Han, Y.-Z. Gui, and G.-C. Guo, Faraday–Michelson system for quantum cryptography, Opt. Lett. **30**, 2632 (2005).

[11] T. Brougham, S. M. Barnett, K. T. McCusker, P. G. Kwiat, and D. J. Gauthier, Security of high-dimensional quantum key distribution protocols using Franson interferometers, J. Phys. B **46**, 104010 (2013).

[12] D. Dequal, L. T. Vidarte, V. R. Rodriguez, G. Vallone, P. Villoresi, A. Leverrier, and E. Diamanti, Feasibility of satellite-to-ground continuous-variable quantum key distribution, npj Quantum Inf. **7**, 3 (2021).

[13] M. Li, T. Wang, J. Han, Z. Yu, M. Cvijetic, H. Ye, and Y. Liu, Free space continuous-variable quantum key distribution with practical links, J. Opt. Soc. Am. B **37**, 3690 (2020).

[14] V. C. Usenko, C. Peuntinger, B. Heim, K. Günthner, I. Derkach, D. Elser, C. Marquardt, R. Filip, and G. Leuchs, Stabilization of transmittance fluctuations caused by beam wandering in continuous-variable quantum communication over free-space atmospheric channels, Opt. Express **26**, 31106 (2018).

[15] Q. Liao, H. Liu, Y. Gong, Z. Wang, Q. Peng, and Y. Guo, Practical continuous-variable quantum secret sharing using plug-and-play dual-phase modulation, Opt. Express **30**, 3876 (2022).

[16] T. Wang, M. Li, and X. Wang, Security analysis of discretized polar modulation continuous-variable quantum key distribution, Opt. Express **30**, 36122 (2022).

[17] Y. Pan, H. Wang, Y. Shao, Y. Pi, T. Ye, Y. Li, W. Huang, and B. Xu, Simple and fast polarization tracking algorithm for continuous-variable quantum key distribution system, in *Optical Fiber Communication Conference* (Optica Publishing Group, Massachusetts Ave. NW, Washington, DC, 2023), pp. Th3J–4.

[18] G. Zhang *et al.*, An integrated silicon photonic chip platform for continuous-variable quantum key distribution, Nat. Photonics **13**, 839 (2019).

[19] X. Wu, Y. Wang, S. Li, W. Zhang, D. Huang, and Y. Guo, Security analysis of passive measurement-device-independent continuous-variable quantum key distribution with almost no public communication, Quantum Inf. Process. **18**, 1 (2019).

[20] W. Ye, H. Zhong, X. Wu, L. Hu, and Y. Guo, Continuous-variable measurement-device-independent quantum key distribution via quantum catalysis, Quantum Inf. Process. **19**, 1 (2020).

[21] D. B. S. Soh, C. Brif, P. J. Coles, N. Lütkenhaus, R. M. Camacho, J. Urayama, and M. Sarovar, Self-referenced continuous-variable quantum key distribution protocol, Phys. Rev. X **5**, 041010 (2015).

[22] N. Jain *et al.*, Practical continuous-variable quantum key distribution with composable security, Nat. Commun. **13**, 4740 (2022).

[23] G. Lindblad, Completely positive maps and entropy inequalities, Commun. Math. Phys. **40**, 147 (1975).

[24] R. Omnès, General theory of the decoherence effect in quantum mechanics, Phys. Rev. A **56**, 3383 (1997).

[25] W. H. Zurek, Decoherence, einselection, and the quantum origins of the classical, Rev. Mod. Phys. **75**, 715 (2003).

[26] H. Carmichael, *An Open Systems Approach to Quantum Optics* (Springer, Berlin, 1993), p. 179.

[27] D. Lidar and W. K. Birgitta, Decoherence-free subspaces and subsystems, in *Irreversible Quantum Dynamics*, edited by F. Benatti and R. Floreanini, Lecture Notes in Physics, Vol. 622 (Springer, Berlin, 2003), pp. 83–120.

[28] G. P. Miroshnichenko, Hamiltonian of photons in a single-mode optical fiber for quantum communications protocols, Opt. Spectrosc. **112**, 777 (2012).

[29] G. Miroshnichenko, Decoherence of a one-photon packet in an imperfect optical fiber, Bull. Russ. Acad. Sci.: Phys. **82**, 1550 (2018).

[30] A. Rivas and A. Luis, SU(2)-invariant depolarization of quantum states of light, Phys. Rev. A **88**, 052120 (2013).

[31] A. Kozubov, A. Gaidash, and G. Miroshnichenko, Quantum model of decoherence in the polarization domain for the fiber channel, Phys. Rev. A **99**, 053842 (2019).

[32] A. Gaidash, A. Kozubov, and G. Miroshnichenko, Dissipative dynamics of quantum states in the fiber channel, Phys. Rev. A **102**, 023711 (2020).

[33] A. Gaidash, A. Kozubov, G. Miroshnichenko, and A. D. Kiselev, Quantum dynamics of mixed polarization states: Effects of environment-mediated intermode coupling, J. Opt. Soc. Am. B **38**, 2603 (2021).

[34] H.-M. Chin, A. A. Hajomer, N. Jain, U. L. Andersen, and T. Gehring, Machine learning based joint polarization and phase compensation for CV-QKD, in *Optical Fiber Communication Conference* (Optica Publishing Group, Massachusetts Ave. NW, Washington, DC, USA, 2023), pp. Th3J–2.

[35] W. Liu, Y. Cao, X. Wang, and Y. Li, Continuous-variable quantum key distribution under strong channel polarization disturbance, Phys. Rev. A **102**, 032625 (2020).

[36] D. Pereira, A. N. Pinto, and N. A. Silva, Polarization diverse true heterodyne receiver architecture for continuous variable quantum key distribution, J. Lightwave Technol. **41**, 432 (2022).

[37] A. Gaidash, A. Kozubov, S. Medvedeva, and G. Miroshnichenko, The influence of signal polarization on quantum bit error rate for subcarrier wave quantum key distribution protocol, Entropy **22**, 1393 (2020).

[38] R. J. Glauber, Coherent and incoherent states of the radiation field, Phys. Rev. **131**, 2766 (1963).

[39] E. Sudarshan, Equivalence of semiclassical and quantum mechanical descriptions of statistical light beams, Phys. Rev. Lett. **10**, 277 (1963).

[40] G. Lindblad, On the generators of quantum dynamical semigroups, Commun. Math. Phys. **48**, 119 (1976).

[41] V. Gorini, A. Kossakowski, and E. C. G. Sudarshan, Completely positive dynamical semigroups of N-level systems, J. Math. Phys. **17**, 821 (1976).

[42] W. P. Schleich, *Quantum Optics in Phase Space* (Wiley, Hoboken, NJ, 2011).

[43] A. D. Kiselev, R. Ali, and A. V. Rybin, Lindblad dynamics and disentanglement in multi-mode bosonic systems, Entropy **23**, 1409 (2021).

[44] D. Huang, P. Huang, D. Lin, and G. Zeng, Long-distance continuous-variable quantum key distribution by controlling excess noise, Sci. Rep. **6**, 19201 (2016).

[45] S. Fossier, E. Diamanti, T. Debuisschert, A. Villing, R. Tualle-Brouri, and P. Grangier, Field test of a continuous-variable quantum key distribution prototype, New J. Phys. **11**, 045023 (2009).

[46] W. Vogel and J. Grabow, Statistics of difference events in homodyne detection, Phys. Rev. A **47**, 4227 (1993).

[47] W. Vogel and D.-G. Welsch, *Quantum Optics* (Wiley, Hoboken, NJ, 2006).

[48] A. Serafini, *Quantum continuous variables: a primer of theoretical methods* (CRC Press, Boca Raton, FL, 2023).

[49] F. Minganti, A. Miranowicz, R. W. Chhajlany, and F. Nori, Quantum exceptional points of non-hermitian Hamiltonians and Liouvillians: The effects of quantum jumps, Phys. Rev. A **100**, 062131 (2019).

[50] Z. Li, Y.-C. Zhang, F. Xu, X. Peng, and H. Guo, Continuous-variable measurement-device-independent quantum key distribution, Phys. Rev. A **89**, 052301 (2014).

[51] E. Diamanti and A. Leverrier, Distributing secret keys with quantum continuous variables: Principle, security and implementations, Entropy **17**, 6072 (2015).

[52] C. Lupo, C. Ottaviani, P. Papanastasiou, and S. Pirandola, Continuous-variable measurement-device-independent quantum key distribution: Composable security against coherent attacks, Phys. Rev. A **97**, 052327 (2018).

[53] S. Pirandola, J. Eisert, C. Weedbrook, A. Furusawa, and S. L. Braunstein, Advances in quantum teleportation, Nat. Photonics **9**, 641 (2015).

[54] Y.-C. Zhang, Z. Li, S. Yu, W. Gu, X. Peng, and H. Guo, Continuous-variable measurement-device-independent quantum key distribution using squeezed states, Phys. Rev. A **90**, 052325 (2014).

[55] Y. Tian, P. Wang, J. Liu, S. Du, W. Liu, Z. Lu, X. Wang, and Y. Li, Experimental demonstration of continuous-variable measurement-device-independent quantum key distribution over optical fiber, Optica **9**, 492 (2022).

[56] L. Fan, Y. Bian, M. Wu, Y. Zhang, and S. Yu, Quantum hacking against discrete-modulated continuous-variable quantum key distribution using modified local oscillator intensity attack with random fluctuations, Phys. Rev. Appl. **20**, 024073 (2023).